Optical Materials 156 (2024) 115948

Contents lists available at ScienceDirect

Optical Materials

journal homepage: www.elsevier.com/locate/optmat

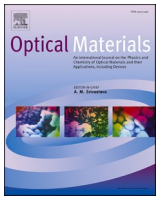

Research Article

Bicontinuous oxide heterostructures based on mixed zinc oxide/tin dioxide film for high photoconductivity

Qais M. Al-Bataineh [a,b,*], Ahmad A. Ahmad [b,**], Lina A. Alakhras [b], Mohammad A. Alebrahim [c], Ahmad Telfah [d]

[a] Experimental Physics, TU Dortmund University, 44227, Dortmund, Germany
[b] Department of Physics, Jordan University of Science and Technology, P.O. Box 3030, Irbid, 22110, Jordan
[c] Department of Applied Medical Sciences, Faculty of Applied Medical Sciences, Jordan University of Science and Technology, Irbid, P.O. Box 3030, 22110, Jordan
[d] Nanotechnology Center, The University of Jordan, 11942, Amman, Jordan

ARTICLE INFO

Keywords:
Self-assembled bicontinuous oxide heterostructures
Zinc oxide (ZnO)
Tin dioxide (SnO_2)
Photoresponsivity
Photodetector device

ABSTRACT

Here, a bicontinuous oxide heterostructure film based on zinc oxide (ZnO) and tin dioxide (SnO_2) is proposed for effiecient photodetection applications. XRF reveals that mixed ZnO/SnO_2 film contains about equal element percentages of Zn (43.8 %) and Sn (41.7 %). XRD and SEM confirm the superior crystallinity of the heterostructure of the mixed ZnO/SnO_2 film. The bandgap energies of ZnO and SnO_2 films are calculated to be 3.17 eV and 3.31 eV. On the other hand, the mixed ZnO/SnO_2 heterostructure film has a lower bandgap energy of 2.92 eV, which can be attributed to the fact that the heterostructure can generate the electron from the valence band of SnO_2, and the holes could assemble at the conduction band of ZnO. The photoresponsivity of mixed ZnO/SnO_2 film is higher than that of pure ZnO and pure SnO_2 films. Additionally, the current of mixed ZnO/SnO_2 film as a function of time exhibits good consistency and repeatability with rectangular profiles. It can be concluded that mixed ZnO/SnO_2 film is considered a potential candidate for photodetector devices.

1. Introduction

Composite materials exhibit superior properties compared to their constituent materials and benefit from functional enhancement resulting from adding a second phase. During fabrication, it is typical to mix phases with desirable dimensions and sizes to achieve the desired properties. Therefore, the attainment of improved properties depends on the control of material distribution [1].

Self-assembled bicontinuous oxide heterostructures are composed of two different oxides arranged in a bicontinuous pattern, which exhibit unique electronic, optical, and magnetic properties [2]. This results in a continuous network of one oxide phase fully interconnected with a continuous network of the other oxide phase, providing a high interfacial area between the two materials. The self-assembly of bicontinuous oxide heterostructures is achieved through the precise control of deposition parameters, such as temperature, pressure, and chemical composition, during the fabrication process [3].

The main critical property of the self-assembled bicontinuous oxide heterostructures is the presence of a bicontinuous network structure, where the two different oxide phases are arranged in a highly interconnected pattern [4]. Compared to their constituents, these heterostructures exhibit exciting properties, such as improved catalytic activity, electrical conductivity, photoelectrical activity, and optical properties [5]. K. Kim and J. Moon [6] reported three-dimensional photoanodes based on bicontinuous $BiVO_4$/ZnO structure for high solar water splitting performance at low bias potential. P. Shao et al. [1] reported a bicontinuous SnO_2/NiO nanocomposite deposited via pulsed laser deposition for high efficiency of solar cells and photodetector devices.

Zinc oxide (ZnO) has been subjected to comprehensive studies due to its distinguishing characteristics, including wide direct bandgap energy, high transparency in the visible region, high exciting binding energy, high thermal and chemical stability, and high semiconductor resistivity [5,7–10]. These properties make the ZnO suitable for the development of technological devices, such as optoelectronics [11,12], LED [13], solar cells [14–16], sensors [17], and other optical coating applications

* Corresponding author. Experimental Physics, TU Dortmund University, 44227, Dortmund, Germany.
** Corresponding author.
E-mail addresses: qais.albataineh@tu-dortmund.de (Q.M. Al-Bataineh), sema@just.edu.jo (A.A. Ahmad).

https://doi.org/10.1016/j.optmat.2024.115948
Received 21 May 2024; Received in revised form 27 July 2024; Accepted 8 August 2024
Available online 9 August 2024

[18]. On the other hand, Tin dioxide (SnO_2) has a wide direct bandgap (3.60 eV), high electrical conductivity, and a tetragonal rutile structure brought on by oxygen vacancies [19]. These properties make the SnO_2 suitable for the development of technological devices, such as opto-electronics [20,21], sensors [22,23], and photocatalysts [24].

In this study, a self-assembled bicontinuous oxide heterostructure based on ZnO/SnO_2 film was synthesized using the simple sol-gel method. The reason for selecting the ZnO/SnO_2 system as the model system for self-assembled bicontinuous oxide heterostructures is the difference in the crystal structure, where the ZnO has hexagonal wurtzite structure [25,26] and the SnO_2 has tetragonal structure [27,28]. Moreover, they are both structurally compatible with ITO substrates. Additionally, the ZnO/SnO_2 system reveals excellent potential in device applications such as gas sensors [29,30], photocatalysts [31,32], energy conversion [33,34], and photodetectors [35,36]. Moreover, one of the best strategies to reduce the recombination of electron-hole pairs is to combine two semiconductors with varying bandgap widths [37]. Therefore, the crystal, chemical, and surface structures of the bicontinuous oxide heterostructure based on ZnO/SnO_2 film were full characterized. After that, the optical, optoelectronic, electrical, and photoelectrical properties of a bicontinuous oxide heterostructure based on ZnO/SnO_2 film were investigated. Therefore, it can be concluded that mixed ZnO/SnO_2 film is considered a potential candidate for UV-photodetector devices.

2. Methods

2.1. Synthesis of mixed oxide solution

The pure ZnO solution was prepared by mixing zinc nitrate hexahydrate (4.38 g, $Zn(NO_3).6H_2O$, Sigma-Aldrich), hexamethylenetetramine (2.80 g, $(CH_2).6N_4$), Sigma-Aldrich), and distilled water (50 mL) under continuous stirring for 2 h. After that, the mixed solution is transferred to an autoclave at a temperature of 95 °C for 6 h [38]. On the other hand, the pure SnO_2 solution was prepared by mixing tin (II) chloride (4.38 g, $SnCl_2$, Sigma-Aldrich) and absolute ethanol (50 mL, ≥99.5 %, Sigma-Aldrich) under continuous stirring for 6 h until it yields a transparent homogeneous solution [39]. After that, the final solutions were filtrated with 0.45 μm filter paper before use. ZnO/SnO_2 mixed oxide solution (0.50:0.50) was prepared by mixing pure ZnO solution (20 mL) with pure SnO_2 solution (20 mL) under continuous stirring for 24 h.

2.2. Deposition of mixed oxide films

Before film deposition, ITO glass substrates (250 nm ITO on glass) were cleaned by sonicating in acetone and isopropyl alcohol for 30 min at ambient conditions. The single layer of pure ZnO, pure SnO_2, and mixed ZnO/SnO_2 films were deposited on clean ITO substrates by immersing them in the final solutions for 2 h. The three film samples were dried in an oven at 110 °C for 30 min. Finally, the three film samples were annealed in an oven at 500 °C for 2 h to get crystalline oxide films [40,41]. The oxide films have an average thickness of 500 nm, measured by a cross-sectional view of SEM micrographs (Fig. 1a).

2.3. Characterizations of mixed oxide films

All measurements were performed at ambient conditions. The structural, elemental, and morphological characterizations were studied using an FTIR spectrometer (Bruker Tensor 27), XRD instrument (Malvern Panalytical Ltd, Malvern, UK), XRF (NEX QC + QuantEZ, Rigaku), and SEM (FEI Quanta FEG 450). In addition, the electrical conductivity was measured by a Keithley 2450 source meter connected with a 4-point probe station (Microworld Inc.). Optical transmittance and reflectance measurements were performed using a UV–Vis spectrophotometer (U–3900H).

The I–V characteristics and UV sensing (in a dark box and under UV illumination conditions) were measured using a UV lamp (365 nm, ~4.0 μW). The photodetector device was composed of ZnO, SnO_2, and ZnO/SnO_2 films deposited on the ITO substrates and covered by the silver paint layer to provide an Ohmic contact to the device. Finally, the I–V characteristics were measured in the dark and under UV illumination using a Keithley 2450 source meter (Fig. 1b).

3. Result and discussion

The synthesis methods of pure ZnO, pure SnO_2, and mixed ZnO/SnO_2 films are detailed in the experimental details section. X-ray fluorescence and FTIR spectroscopy investigate the chemical structure and the sample quality. Fig. 2a illustrates the typical XRF scans of pure ZnO, pure SnO_2, and mixed ZnO/SnO_2 films. The pure ZnO and pure SnO_2 films have Zn and Sn element percentages of 96.5 % and 70.2 %, respectively. The

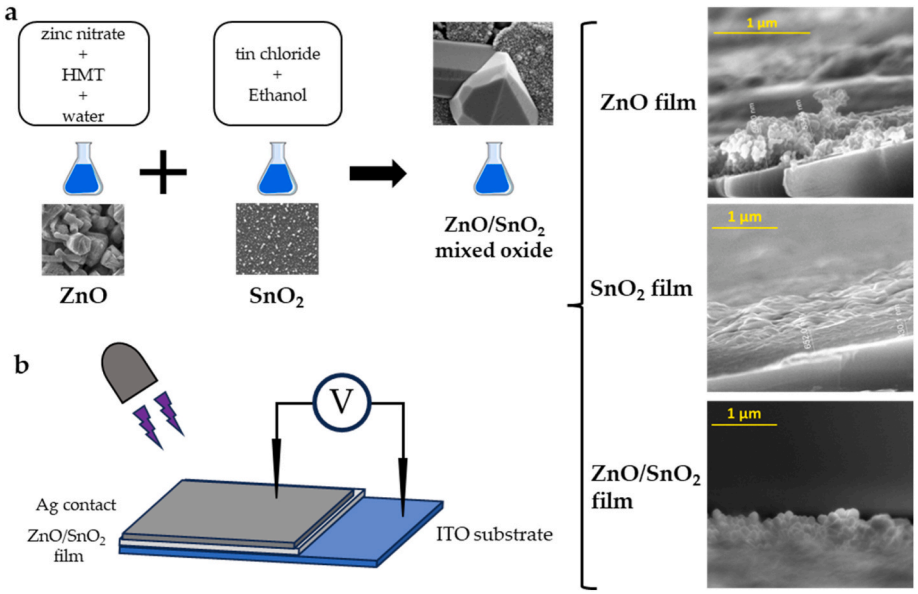

Fig. 1. **(a)** Schematic diagram of deposition process. **(b)** Schematic representation of the fabricated devices.

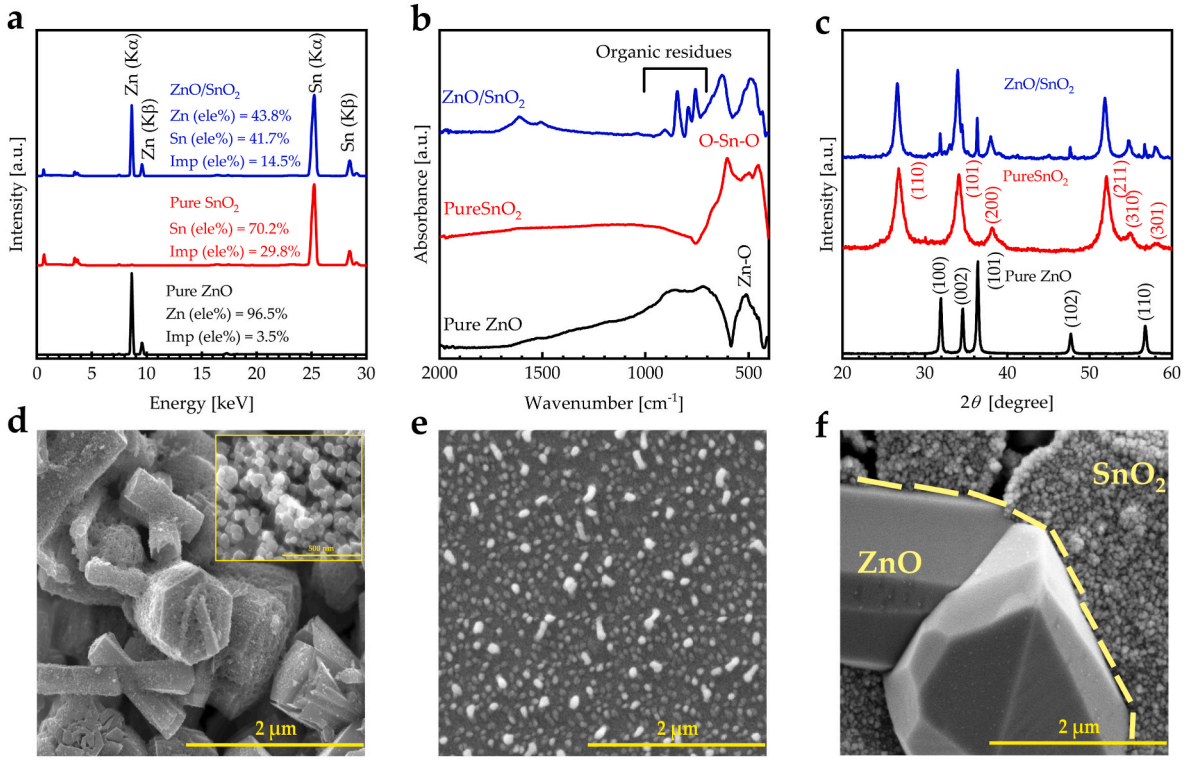

Fig. 2. **(a)** XRF scans, **(b)** FTIR spectra, and **(c)** XRD patterns of pure ZnO, pure SnO_2, and mixed ZnO/SnO_2 films, SEM micrographs of **(d)** pure ZnO film with inset with scale of 500 nm, **(e)** pure SnO2 film, and **(f)** mixed ZnO/SnO_2 film.

other element percentages represent the organic impurities, as seen in FTIR spectra (Fig. 2b). In addition, the mixed ZnO/SnO_2 film contains about equal element percentages of Zn (43.8 %) and Sn (41.7 %), confirming the equal concentrations of ZnO and SnO_2 in the ZnO/SnO_2 film.

The structural analysis was conducted using XRD patterns and SEM micrographs to confirm the heterostructure of the mixed ZnO/SnO_2 film. Fig. 2c illustrates the typical XRD patterns of pure ZnO, pure SnO_2, and mixed ZnO/SnO_2 films in 2θ mode. Pure ZnO film exhibits different diffraction angles located at 31.74°, 34.38°, 36.22°, 47.53°, and 56.60° representing the Miller indices for (100), (002), (101), (102), and (110) of a polycrystalline hexagonal wurtzite structure of ZnO (JCPDS 36–1451), respectively. On the other hand, Pure SnO_2 film exhibits different diffraction angles located at 26.85°, 34.13°, 38.21°, 52.07°, 54.38°, and 58.13° representing the Miller indices for (110), (101), (200), (211), (310), and (301) of a polycrystalline tetragonal structure of SnO_2 (JCPDS 41–1445). Compared to the pure ZnO and pure SnO_2, the co-existence of both diffraction peaks for ZnO and SnO_2 provides a single out-of-plane orientation of mixed ZnO/SnO_2 films. More specifically, SnO_2(101) and ZnO(002) diffraction peaks show different linewidth values of 0.53° and 0.20°, respectively, confirming the superior crystallinity of the heterostructure of the mixed ZnO/SnO_2 film. Additionally, we can demonstrate the superior crystallinity of the heterostructure by studying the lattice constants of the oxide films. The ZnO film has lattice constants of $a = 3.24$ Å and $c = 5.19$ Å, whereas the SnO_2 film has lattice constants of $a = 4.71$ Å and $c = 3.17$ Å. Mixed ZnO/SnO_2 film has two phases of hexagonal ZnO with $a = 3.24$ Å and $c = 5.19$ Å and tetragonal SnO_2 with $a = 4.74$ Å and $c = 3.18$ Å (Table 1). The lattice constants of ZnO and SnO_2 crystals are agreed with the literature [26,38,42,43].

Williamson Hall (WH) method is one of the most common techniques for investigating microstructural properties depending on the XRD pattern, such as crystallite size D and microstrain ε. Crystallite size and microstrain can be investigated by the modified WH method [44],

Table 1
The Resultant microstructure parameters of pure ZnO, pure SnO_2, and mixed ZnO/SnO_2 films.

Film	Phase	a [Å]	c [Å]	D [nm]	$\varepsilon \times 10^{-3}$
ZnO		3.24	5.19	45	1.04
SnO_2		4.71	3.17	11	5.29
ZnO/SnO_2	ZnO phase	3.24	5.19	47	1.01
	SnO_2 phase	4.74	3.18	11	2.77

$$\beta \cos\theta = \frac{k\lambda}{D} + 4\varepsilon \sin\theta \quad (1)$$

where: β is the full width at half maximum (FWHM) in radians, and k is a dimensionless shape factor equal to 0.94 [45,46]. The crystallite size and microstrain can be calculated using the slope and the intersection with the vertical axis of the linear slope relation between ($\beta \cos\theta$) and ($4 \sin\theta$). The resultant values for the crystallite size D and microstrain ε for pure ZnO, pure SnO_2, and mixed ZnO/SnO_2 films are tabulated in Table 1. The crystallite size for pure ZnO film is about 45 nm, whereas the crystallite size for pure SnO_2 film is about 11 nm. Additionally, mixed ZnO/SnO_2 film has two phases; the hexagonal ZnO phase has a crystallite size of 24 nm, while the tetragonal SnO_2 phase has a crystallite size of 11 nm. The crystallite size of both ZnO and SnO_2 films is the same as ZnO and SnO_2 in the mixed ZnO/SnO_2 film, confirming the superior crystallinity of the heterostructure of the mixed ZnO/SnO_2 film.

The surface morphology of pure ZnO, pure SnO_2, and mixed ZnO/SnO_2 films is investigated by scanning electron microscope (SEM). Pure ZnO film exhibits hexagonal rod-patterned formation (Fig. 2d) [47]. Additionally, pure SnO_2 film reveals the uniform distribution of small tetragonal grains (Fig. 2e). On the other hand, mixed ZnO/SnO_2 film reveals a heterostructure of mixed ZnO phase and SnO_2, in which the ZnO phase exhibits a hexagonal rod pattern, while the SnO_2 phase exhibits the distribution of small grains (Fig. 2f). SEM micrographs show

that the hexagonal ZnO rods in the mixed ZnO/SnO_2 films are larger than the hexagonal ZnO rods in pure ZnO, and in contrast, the ZnO has the same crystallite size value for the two films. This can be attributed to the fact that the ZnO nanorods contain small ZnO nanoparticles that form the large ZnO nanorods, indicating that the larger ZnO nanorods mean more ZnO nanoparticles agglomeration (The inset in Fig. 2d).

Electrical conductivity maps of films can provide information on the spatial distribution of the electrical conductivity across the film surface. Typically, electrical conductivity maps of pure ZnO, pure SnO_2, and mixed ZnO/SnO_2 films show regions of varying conductivity, which can be related to the distribution of ZnO and SnO_2 in the film. The electrical conductivity map of ZnO film shows a homogeneous distribution of electrical conductivity values with an average conductivity value of 0.13 S cm^{-1} (Fig. 3a). Additionally, the electrical conductivity map of SnO_2 film shows a homogeneous distribution of electrical conductivity values with an average conductivity value of 56.26 S cm^{-1} (Fig. 3b). Mixed ZnO/SnO_2 film shows the co-existence of the SnO_2 region at higher conductivity values region and the ZnO region at lower conductivity values region (Fig. 3c), confirming the superior crystallinity of heterostructure of the mixed ZnO/SnO_2 film.

The transmittance spectra of pure ZnO, pure SnO_2, and mixed ZnO/SnO_2 films are illustrated in Fig. 4a. The transmittance spectrum of pure ZnO film demonstrates a sudden rise from 0 % to 72 % as incident light wavelength increases from 300 nm to 400 nm. Then, the transmittance values increase slightly from 72 % to 78 % as incident light wavelength increases from 400 nm to 700 nm. The existence of a small shoulder in the transmittance spectrum of ZnO film at 356 nm confirms the presence of the excitonic absorption characteristics [40]. On the other hand, the transmittance spectrum of pure SnO_2 film demonstrates a sudden rise from 0 % to 60 % as incident light wavelength increases from 300 nm to 365 nm. Then, the transmittance values increase slightly from 60 % to 73 % as incident light wavelength increases from 365 nm to 700 nm. Additionally, the transmittance spectra of mixed ZnO/SnO_2 film have the same behavior as pure ZnO film with lower transmittance values, in addition to shifting in the absorption edge into the red region, which means a significant reduction in the bandgap energy of the mixed oxide films.

The extinction coefficient spectra (k) are calculated using $k = \alpha\lambda/4\pi$, where λ is the incident light wavelength, and α is the absorption coefficient, which can be given by $\alpha = (1/d)\ln((1-R)/T)$, with d is the film thickness ($d \approx 500\,nm$) [8]. Before the absorption edge, a sharp decrease in extinction coefficient values was observed. Then, lower extinction coefficient values in the visible light for all film samples show that oxide films can permit visible light to pass through with low loss (Fig. 4b). The refractive index spectra (n) are calculated using $n = (1+R/1-R) + \sqrt{\left(4R/(1-R)^2\right) - k^2}$ [41,48]. Fig. 4c illustrates the refractive index spectra for pure ZnO, pure SnO_2, and mixed ZnO/SnO_2 films. The refractive index spectra of all oxide films are divided into two regions. The first region before 400 nm exhibits an anomalous dispersion behavior, in which the photon-electron coupling occurs [49]. On the other hand, at $\lambda > 400$ nm, the refractive index spectra exhibit normal dispersion behavior. The refractive index values of mixed ZnO/SnO_2 film is higher than pure ZnO and pure SnO_2 films, which can be attributed to the interference regions between the ZnO region and SnO_2 region, increasing the light scattered at these interfaces.

The photoconversion process of mixed ZnO/SnO_2 film, including light absorption, photocarrier generation, transportation, and transportation, was investigated due to the existence of charge interactions at the interfaces of ZnO/SnO_2. First, Tauc plots were produced to investigate the bandgap energy (E_g) of pure ZnO, pure SnO_2, and mixed ZnO/SnO_2 films by plotting $(\alpha h\nu)^2$ on the y-axis versus $h\nu$ on the x-axis, according to the equation $(\alpha h\nu)^2 = \beta(h\nu - E_g)$ for direct bandgap semiconductors [50]. The bandgap energies of ZnO and SnO_2 films are calculated to be 3.17 eV and 3.31 eV based on the Tauc plot method. The band structure, including the E_{VB}, E_{CB}, and bandgap energy, were investigated using the ionization energy and the electron affinity energy, according to the literature [51,52]. The band diagram of the ZnO and SnO_2 films is illustrated in Fig. 5a. Additionally, the mixed ZnO/SnO_2 heterostructure film has a lower bandgap energy of 2.92 eV. S. Bibi et al. [53] show that the bandgap energy of ZnO/SnO_2 binary films increases linearly from 3.37 for pure ZnO film to 3.65 eV for pure SnO_2 film. In addition, L. Xu et al. [54] show that the bandgaps of pure ZnO and SnO_2 films are 3.26 and 3.91 eV, respectively; the optical bandgaps of ZnSnO films are between the bandgap energies of ZnO and SnO_2. Therefore, the bandgap energy of ZnO/SnO_2 binary films is found to be between the individual ZnO and SnO_2 films. In contrast, the bandgap energy of ZnO/SnO_2 bicontinuous heterostructure films is lower than ZnO and SnO_2 films, which can be attributed to the fact that the heterostructure can generate the electron from the valence band of SnO_2. At the same time, the holes could assemble at the conduction band of ZnO (Fig. 5a), which is in agreement to P. Shao et al. study [1].

Current-voltage (IV) curves of pure ZnO, pure SnO_2, and mixed ZnO/SnO_2 films measured in the dark and under UV irradiation with a wavelength of 365 nm and power of ~4.0 μW through ±3 V bias voltage is illustrated in Fig. 5b, c, d. All IV curves exhibit a semi-Schottky behavior by alternating bias voltage from −3 to 3 V due to the existence of large defect concentrations across the films [55,56]. The current in all samples increases with both the forward and the reverse voltage under UV light. This can be attributed to the adsorption of oxygen molecules by metal oxide film in the dark. Consequently, the free surface electrons are trapped, and the carrier's mobility decreases. On the other hand, after UV irradiation, high-energy photons are absorbed by the metal oxide film, and many hole-electron pairs are generated, consequently increasing the free carriers concentration [57].

Mixed ZnO/SnO_2 film demonstrates a higher distinction between

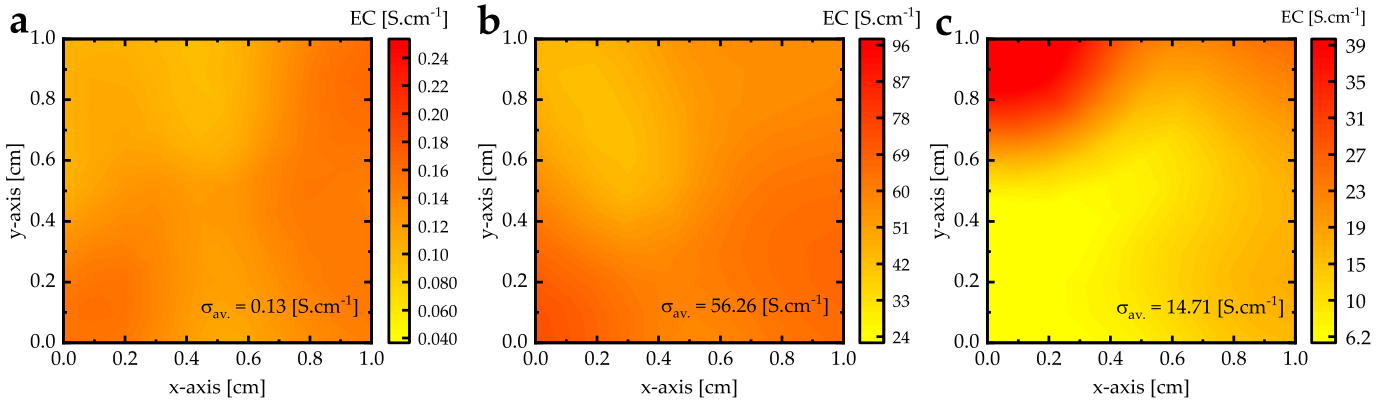

Fig. 3. Electrical conductivity maps of **(a)** pure ZnO film, **(b)** pure SnO_2 film, and **(c)** mixed ZnO/SnO_2 film.

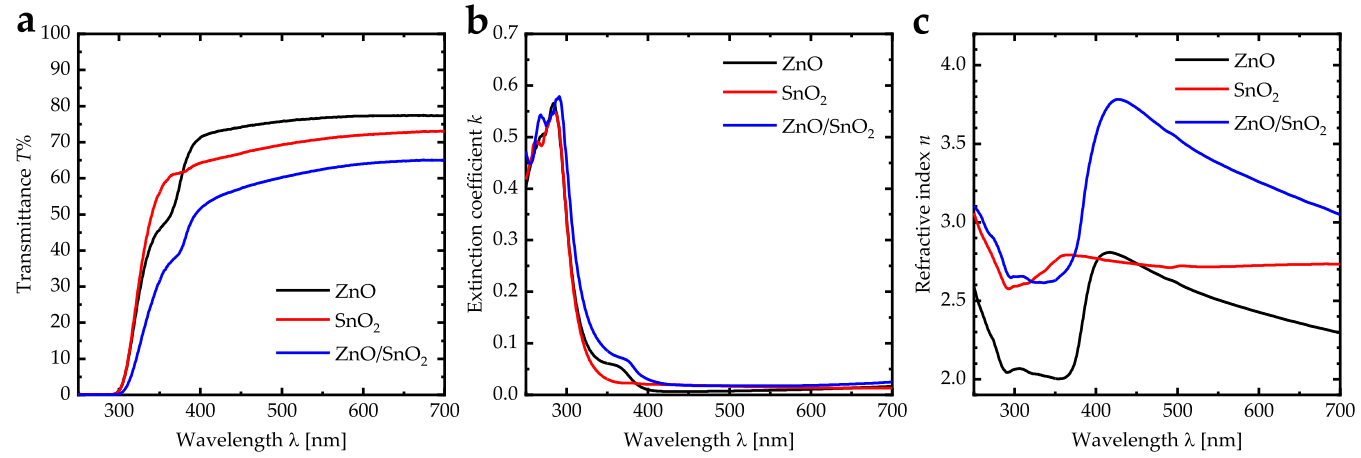

Fig. 4. **(a)** Transmittance, **(b)** extinction coefficient, and **(c)** refractive index spectra for pure ZnO, pure SnO_2, and mixed ZnO/SnO_2 films.

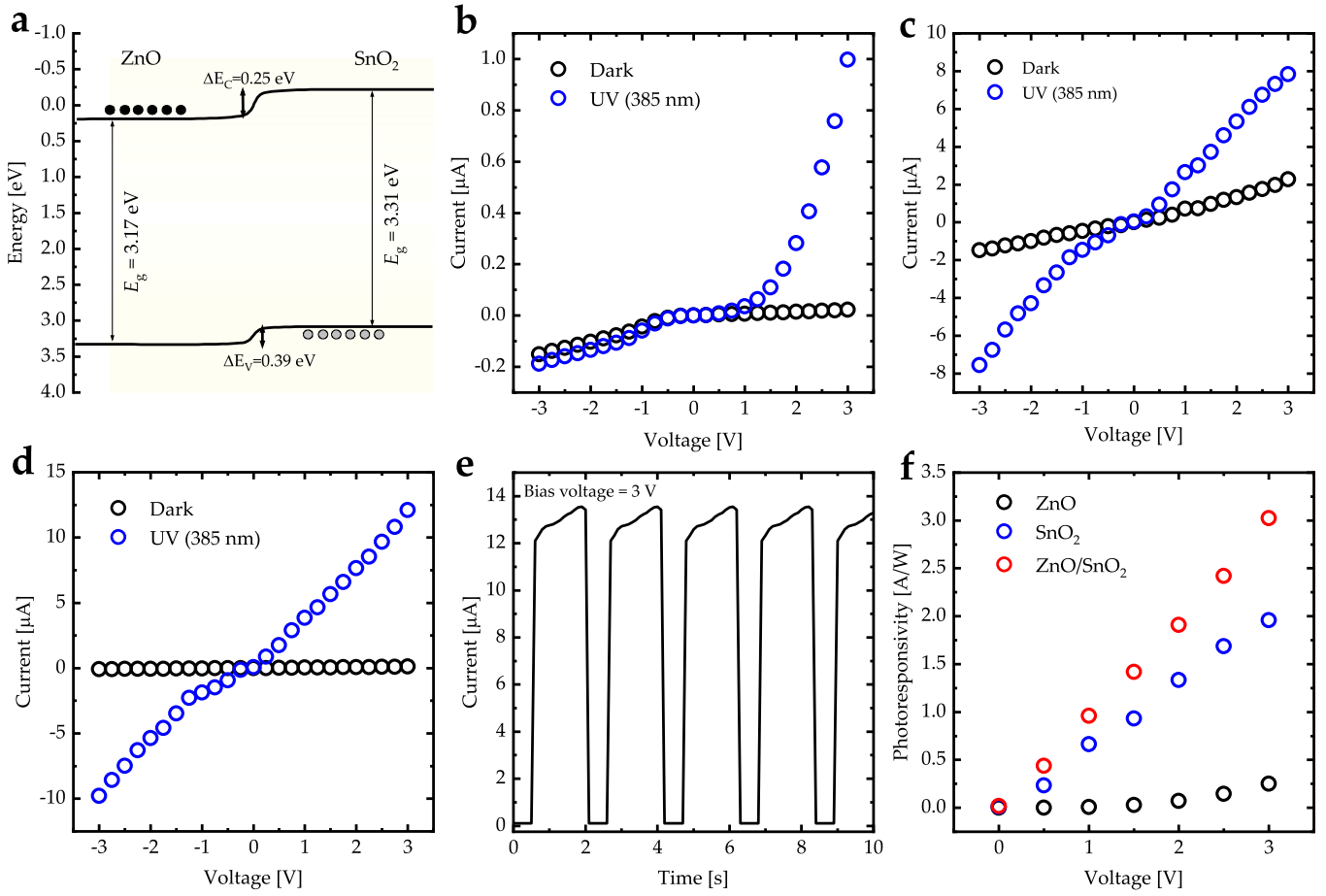

Fig. 5. **(a)** Band diagram of pure ZnO and pure SnO_2 films estimated by optical properties, electron affinity, and first ionization energy. I–V characteristics of **(b)** pure ZnO, **(c)** pure SnO_2, and **(d)** mixed ZnO/SnO_2 films based on UV photodetector measured in the dark and under UV light. **(e)** The photocurrent response curve of ZnO/SnO_2 film irradiated by UV-light (365 nm) at an applied bias voltage of 3 V. **(f)** Photoresponsivity of pure ZnO, pure SnO_2, and mixed ZnO/SnO_2 films based UV photodetector.

dark current and photocurrent compared to pure ZnO and pure SnO_2 films. For instance, at a bias voltage of 3 V, the distinctions between dark current and photocurrent ZnO and SnO_2 films are 0.97 μA and 5.55 μA, respectively (Fig. 5b and c). On the other hand, the distinction between dark current and photocurrent of mixed ZnO/SnO_2 film is 12.00 μA (Fig. 5d). The current of mixed ZnO/SnO_2 film as a function of time at a bias voltage of 3 V is used to investigate the photocurrent response in on/off states (Fig. 5e). The current of mixed ZnO/SnO_2 film as a function of time exhibits good consistency and repeatability with rectangular profiles. There are two primary components that make up the response time of the mixed ZnO/SnO_2 film rising time of about 0.58 s and a decaying time of about 0.13 s. The photoresponsivity of pure ZnO, pure

SnO_2, and mixed ZnO/SnO_2 films can be calculated using $Resp. = I_{ph}/P_0$ [A/W] (Fig. 5f) [58]. The photoresponsivity of mixed ZnO/SnO_2 film is higher than that of pure ZnO and pure SnO_2 films, which can be attributed to the fact that the heterostructure can generate the electron from the valence band of SnO_2. At the same time, the holes could assemble at the conduction band of ZnO. In addition, The photoresposivity of the proposed mixed ZnO/SnO2 film is higher than NiO/ZnO heterojunction photodetector [59], ZnO nanorods [60], Cu^{2+} doped ZnS/ZnO nanorods [60], and SnO_2 film [61].

4. Conclusions

This study demonstrates a self-assembled bicontinuous oxide heterostructure based on ZnO/SnO_2 film. XRF indicated that the mixed ZnO/SnO_2 film contains equal concentrations of Zn and Sn elements. XRD reveals the superior crystallinity of the heterostructure of the mixed ZnO/SnO_2 film by investigating the diffraction peaks and lattice constants. More specifically, SnO_2(101) and ZnO(002) diffraction peaks show different linewidth values of 0.53° and 0.20°, respectively. In addition, the SEM image of mixed ZnO/SnO_2 film reveals a heterostructure of mixed ZnO phase and SnO_2, in which the ZnO phase exhibits a hexagonal rod pattern, while the SnO_2 phase exhibits the distribution of small grains. The electrical conductivity map of mixed ZnO/SnO_2 film also confirms the bicontinuous oxide heterostructure due to the coexistence of the SnO_2 region at higher conductivity values region and the ZnO region at lower conductivity values region. The bandgap energies of ZnO and SnO_2 films are calculated to be 3.17 eV and 3.31 eV based on the Tauc plot method. On the other hand, the mixed ZnO/SnO_2 heterostructure film has a lower bandgap energy of 2.92 eV, which can be attributed to the fact that the heterostructure can generate the electron from the valence band of SnO_2. At the same time, the holes could assemble at the conduction band of ZnO. In addition, mixed ZnO/SnO_2 film demonstrates a higher distinction between dark current and photocurrent compared to pure ZnO and pure SnO_2 films. The current of mixed ZnO/SnO_2 film as a function of time exhibits good consistency and repeatability with rectangular profiles. The photoresponsivity of mixed ZnO/SnO_2 film is higher than that of pure ZnO and pure SnO_2 films, which can be attributed to the fact that the heterostructure can generate the electron from the valence band of SnO_2. At the same time, the holes could assemble at the conduction band of ZnO. Therefore, it can be concluded that mixed ZnO/SnO_2 film is considered a potential candidate for photodetector devices.

Consent to participate

All authors participate in this work.

Consent to publish

All authors agree to publish this work.

CRediT authorship contribution statement

Qais M. Al-Bataineh: Writing – original draft, Methodology, Conceptualization. **Ahmad A. Ahmad:** Writing – review & editing, Funding acquisition, Data curation. **Lina A. Alakhras:** Methodology, Data curation. **Mohammad A. Alebrahim:** Writing – review & editing, Data curation. **Ahmad Telfah:** Writing – review & editing, Supervision, Conceptualization.

Declaration of competing interest

The authors declare no conflict of interest.

Data availability

Data will be made available on request.

Acknowledgement

The scientific support by the Ministerium für Innovation, Wissenschaft und Forschung des Landes Nordrhein-Westfalen, the Senatsverwaltung für Wirtschaft, Technologie und Forschung des LandesBerlin, and the Bundesministerium für Bildung und Forschung is gratefully acknowledged. The authors would like to acknowledge Jordan University of Science and Technology for the supporting offered by the Deanship of Scientific Research (Research # 187/2024). We also thank Prof. Mohammad-Ali H. Al-Akhras for helping our members use the biomedical laboratory.

References

[1] P.-W. Shao, Y.-X. Wu, W.-H. Chen, M. Zhang, M. Dai, Y.-C. Kuo, S.-H. Hsieh, Y.-C. Tang, P.-L. Liu, P. Yu, Bicontinuous oxide heteroepitaxy with enhanced photoconductivity, Nat. Commun. 14 (1) (2023) 21.
[2] Z. Hiroi, H. Hayamizu, T. Yoshida, Y. Muraoka, Y. Okamoto, J.-i. Yamaura, Y. Ueda, Spinodal decomposition in the TiO2–VO2 system, Chem. Mater. 25 (11) (2013) 2202–2210.
[3] W. Zhang, R. Ramesh, J.L. MacManus-Driscoll, H. Wang, Multifunctional, self-assembled oxide nanocomposite thin films and devices, MRS Bull. 40 (9) (2015) 736–745.
[4] J.L. MacManus-Driscoll, Self-assembled heteroepitaxial oxide nanocomposite thin film structures: designing interface-induced functionality in electronic materials, Adv. Funct. Mater. 20 (13) (2010) 2035–2045.
[5] Q.M. Al-Bataineh, M. Telfah, A.A. Ahmad, A.M. Alsaad, I.A. Qattan, H. Baaziz, Z. Charifi, A. Telfah, Synthesis, crystallography, microstructure, crystal defects, optical and optoelectronic properties of ZnO: CeO2 mixed oxide thin films, Photonics 7 (4) (2020) 112. MDPI.
[6] K. Kim, J.H. Moon, Three-dimensional bicontinuous BiVO4/ZnO photoanodes for high solar water-splitting performance at low bias potential, ACS applied materials & interfaces 10 (40) (2018) 34238–34244.
[7] Q.M. Al-Bataineh, A. Alsaad, A. Ahmad, A. Al-Sawalmih, Structural, electronic and optical characterization of ZnO thin film-seeded platforms for ZnO nanostructures: sol–gel method versus ab initio calculations, J. Electron. Mater. 48 (2019) 5028–5038.
[8] A. Ahmad, A. Alsaad, Q. Al-Bataineh, M. Al-Naafa, Optical and structural investigations of dip-synthesized boron-doped ZnO-seeded platforms for ZnO nanostructures, Appl. Phys. A 124 (2018) 1–13.
[9] A. Alsaad, A. Ahmad, I. Qattan, Q.M. Al-Bataineh, Z. Albataineh, Structural, optoelectrical, linear, and nonlinear optical characterizations of dip-synthesized undoped ZnO and group III elements (B, Al, Ga, and In)-doped ZnO thin films, Crystals 10 (4) (2020) 252.
[10] A. Ahmad, A. Alsaad, Q. Al-Bataineh, Optical and Structural Characterization of Dip Synthesized Al-B Co-doped ZnO Seeded Platforms for ZnO Nanostructures, 2017.
[11] E. Muchuweni, T. Sathiaraj, H. Nyakotyo, Synthesis and characterization of zinc oxide thin films for optoelectronic applications, Heliyon 3 (4) (2017) e00285.
[12] G. Malik, S. Mourya, J. Jaiswal, R. Chandra, Effect of annealing parameters on optoelectronic properties of highly ordered ZnO thin films, Mater. Sci. Semicond. Process. 100 (2019) 200–213.
[13] K. Sandeep, S. Bhat, S. Dharmaprakash, Structural, optical, and LED characteristics of ZnO and Al doped ZnO thin films, J. Phys. Chem. Solid. 104 (2017) 36–44.
[14] S.K. Kokate, C.V. Jagtap, P.K. Baviskar, S.R. Jadkar, H.M. Pathan, K.C. Mohite, CdS sensitized cadmium doped ZnO solar cell: fabrication and characterizations, Optik 157 (2018) 628–634.
[15] S. Qiao, J. Liu, G. Fu, K. Ren, Z. Li, S. Wang, C. Pan, ZnO nanowire based CIGS solar cell and its efficiency enhancement by the piezo-phototronic effect, Nano Energy 49 (2018) 508–514.
[16] I. Dhahri, M. Ellouze, S. Labidi, Q.M. Al-Bataineh, J. Etzkorn, H. Guermazi, A. Telfah, C.J. Tavares, R. Hergenröder, T. Appel, Optical and structural properties of ZnO NPs and ZnO–Bi2O3 nanocomposites, Ceram. Int. 48 (1) (2022) 266–277.
[17] L. Zhu, W. Zeng, Room-temperature gas sensing of ZnO-based gas sensor: a review, Sensor Actuator Phys. 267 (2017) 242–261.
[18] Q.M.A.-B. Mr, T.O.S. Mr, K.A. A.-i. Miss, Optical properties of hydrophobic ZnO nano-structure based on antireflective coatings of ZnO/TiO2/SiO2 thin films, Phys. B Condens. Matter 593 (2020) 412263.
[19] Y. Yang, B. Maeng, D.G. Jung, J. Lee, Y. Kim, J. Kwon, H.K. An, D. Jung, Annealing effects on SnO2 thin film for H2 gas sensing, Nanomaterials 12 (18) (2022) 3227.
[20] E. Pargoletti, U.H. Hossain, I. Di Bernardo, H. Chen, T. Tran-Phu, G.L. Chiarello, J. Lipton-Duffin, V. Pifferi, A. Tricoli, G. Cappelletti, Engineering of SnO2–graphene oxide nanoheterojunctions for selective room-temperature chemical sensing and optoelectronic devices, ACS applied materials & interfaces 12 (35) (2020) 39549–39560.
[21] J. Divya, A. Pramothkumar, H.J.L. Hilary, P.J. Jayanthi, P. Jobe prabakar, Impact of copper (Cu) and iron (Fe) co-doping on structural, optical, magnetic and

electrical properties of tin oxide (SnO2) nanoparticles for optoelectronics applications, J. Mater. Sci. Mater. Electron. 32 (12) (2021) 16775–16785.
[22] B. Li, Q. Zhou, S. Peng, Y. Liao, Recent advances of SnO2-based sensors for detecting volatile organic compounds, Frontiers in chemistry 8 (2020) 321.
[23] Y. Masuda, Recent advances in SnO2 nanostructure based gas sensors, Sensor. Actuator. B Chem. (2022) 131876.
[24] C. Sun, J. Yang, M. Xu, Y. Cui, W. Ren, J. Zhang, H. Zhao, B. Liang, Recent intensification strategies of SnO2-based photocatalysts: a review, Chem. Eng. J. 427 (2022) 131564.
[25] Q.M. Al-Bataineh, W.T. Bani-Hani, A.A. Ahmad, A.M. Alsaad, A.D. Telfah, Promising electrochemical catalytic steel electrodes structure coated by ZnO films for water treatment and water-splitting applications, J. Mater. Sci. Mater. Electron. (2022) 1–11.
[26] Q.M. Al-Bataineh, R. Ababneh, A. Bahti, A.A. Bani-Salameh, C.J. Tavares, A. Telfah, Effect of hydrogen-related shallow donor on the physical and chemical properties of Ag-doped ZnO nanostructures, J. Mater. Sci. Mater. Electron. 33 (22) (2022) 17434–17445.
[27] D. Singh, H. Singh, N. Kumar, N. Aggarwal, A. Kapoor, A. Sharma, D. Saini, Influence of aliovalent V3+ substitution on physicochemical characteristics of tetragonal SnO2 nanoparticles, J. Mater. Sci. Mater. Electron. 34 (9) (2023) 782.
[28] M. El Jouad, T. Garmim, A. Louardi, B. Hartiti, M. Monkade, S. Touhtouh, A. Hajjaji, Elaboration and characterization of Ni and Al co-doped SnO2 thin films prepared by spray pyrolysis technique for photovoltaic applications, Mater. Sci. Eng., B 286 (2022) 116044.
[29] X. Zhang, J. Sun, K. Tang, H. Wang, T. Chen, K. Jiang, T. Zhou, H. Quan, R. Guo, Ultralow detection limit and ultrafast response/recovery of the H2 gas sensor based on Pd-doped rGO/ZnO-SnO2 from hydrothermal synthesis, Microsystems & Nanoengineering 8 (1) (2022) 67.
[30] V.T. Duoc, C.M. Hung, H. Nguyen, N. Van Duy, N. Van Hieu, N.D. Hoa, Room temperature highly toxic NO2 gas sensors based on rootstock/scion nanowires of SnO2/ZnO, ZnO/SnO2, SnO2/SnO2 and, ZnO/ZnO, Sensor. Actuator. B Chem. 348 (2021) 130652.
[31] M.H. Sayadi, S. Ghollasimood, N. Ahmadpour, S. Homaeigohar, Biosynthesis of the ZnO/SnO2 nanoparticles and characterization of their photocatalytic potential for removal of organic water pollutants, Journal of photochemistry and photobiology A: chemistry 425 (2022) 113662.
[32] S. Begum, S.R. Mishra, M. Ahmaruzzaman, Fabrication of ZnO–SnO2 nanocomposite and its photocatalytic activity for enhanced degradation of Biebrich scarlet, Environ. Sci. Pollut. Control Ser. 29 (58) (2022) 87347–87360.
[33] U. Khan, T. Iqbal, M. Khan, R. Wu, SnO2/ZnO as double electron transport layer for halide perovskite solar cells, Sol. Energy 223 (2021) 346–350.
[34] S. Li, J. Pan, H. Li, Y. Liu, W. Ou, J. Wang, C. Song, W. Zhao, Y. Zheng, C. Li, The transparent SnO/ZnO quantum dots/SnO2 pn junction towards the enhancement of photovoltaic conversion, Chem. Eng. J. 366 (2019) 305–312.
[35] Q.-M. Fu, J.-L. Peng, Z.-C. Yao, H.-Y. Zhao, Z.-B. Ma, H. Tao, Y.-F. Tu, Y. Tian, D. Zhou, Y.-B. Han, Highly sensitive ultraviolet photodetectors based on ZnO/SnO2 core-shell nanorod arrays, Appl. Surf. Sci. 527 (2020) 146923.
[36] Y. Fu, L. Guo, Z. Ren, X. Li, Q. Zhang, J. Wu, Y. Li, W. Liu, P. Li, J. Ma, Enhanced property of flexible UV photodetectors based on electrospinning ZnO–SnO2 heterojunction nanofibers by the formation of Zn2SnO4, Ceram. Int. 49 (7) (2023) 11402–11410.
[37] F. Barati, M. Grossnickle, S. Su, R.K. Lake, V. Aji, N.M. Gabor, Hot carrier-enhanced interlayer electron–hole pair multiplication in 2D semiconductor heterostructure photocells, Nat. Nanotechnol. 12 (12) (2017) 1134–1139.
[38] A.A. Ahmad, A.M. Alsaad, I.A. Aljarrah, Q.M. Al-Bataineh, A.D. Telfah, Optical, electronic, and structural properties of different nanostructured ZnO morphologies, The European Physical Journal Plus 137 (6) (2022) 752.
[39] A. Doyan, L. Muliyadi, S. Hakim, M. Taufik, Characteristics and optical properties of fluorine doped SnO2 thin film prepared by a sol–gel spin coating, in: Journal of Physics: Conference Series, IOP Publishing, 2019 012003, 1397, no. 1.
[40] A.A. Ahmad, Q.M. Al-Bataineh, I.A. Aljarrah, A.D. Telfah, Electrochemical degradation of methyl red in zinc hydroxide and zinc oxide thin films, physical and chemical activation, Mater. Chem. Phys. 280 (2022) 125793.
[41] Q.M. Al-Bataineh, A. Alsaad, A. Ahmad, A. Al-Sawalmih, Structural, electronic and optical characterization of ZnO thin film-seeded platforms for ZnO nanostructures: sol–gel method versus ab initio calculations, J. Electron. Mater. 48 (8) (2019) 5028–5038.
[42] S. Moradi, A. Nazari Setayesh, H. Sedghi, A comparative study on the structural and spectroscopic ellipsometry characterizations of (Co, Ni)-doped SnO2 nanostructured films spin-coated on glass substrates, Bull. Mater. Sci. 46 (1) (2022) 5.
[43] P. Senthilkumar, S. Raja, R.R. Babu, G. Vasuki, Enhanced electrical and optoelectronic properties of W doped SnO2 thin films, Opt. Mater. 126 (2022) 112234.
[44] A.A. Al-Ghamdi, O.A. Al-Hartomy, M. El Okr, A. Nawar, S. El-Gazzar, F. El-Tantawy, F. Yakuphanoglu, Semiconducting properties of Al doped ZnO thin films, Spectrochim. Acta Mol. Biomol. Spectrosc. 131 (2014) 512–517.
[45] C. Shull, The determination of X-ray diffraction line widths, Phys. Rev. 70 (9–10) (1946) 679.
[46] R. Pielaszek, Diffraction Studies of Microstructure of Nanocrystals Exposed to High Pressure, Warsaw University, Department of Physics, Warsaw, Poland, 2003. Ph. D. Thesis.
[47] A. Ahmad, A. Migdadi, A. Alsaad, Q.M. Al-Bataineh, A. Telfah, Optical, structural, and morphological characterizations of synthesized (Cd–Ni) co-doped ZnO thin films, Appl. Phys. A 127 (12) (2021) 922.
[48] A. Ahmad, A. Alsaad, Q. Al-Bataineh, M. Al-Naafa, Optical and structural investigations of dip-synthesized boron-doped ZnO-seeded platforms for ZnO nanostructures, Appl. Phys. A 124 (6) (2018) 458.
[49] A. Alsaad, C.M. Marin, N. Alaqtash, H.-W. Chao, T.-H. Chang, C.L. Cheung, A. Ahmad, I. Qattan, R.F. Sabirianov, Crystallographic, vibrational modes and optical properties data of α-DIPAB crystal, Data Brief 16 (2018) 667–684.
[50] A. Ahmad, A. Migdadi, A. Alsaad, Q.M. Al-Bataineh, A. Telfah, Optical, structural, and morphological characterizations of synthesized (Cd–Ni) co-doped ZnO thin films, Appl. Phys. A 127 (12) (2021) 1–12.
[51] A. Hassanien, A.A.J.S. Akl, Microstructures, Effect of Se Addition on Optical and Electrical Properties of Chalcogenide CdSSe Thin Films, vol. 89, 2016, pp. 153–169.
[52] Q.M. Al-Bataineh, A.A. Ahmad, A. Alsaad, A.D.J.H. Telfah, Optical characterizations of PMMA/metal oxide nanoparticles thin films: bandgap engineering using a novel derived model 7 (1) (2021) e05952.
[53] S. Bibi, A. Shah, A. Mahmood, Z. Ali, Q. Raza, U. Aziz, Haneef, A. Waheed, Z. Shah, Synthesis and characterization of binary ZnO–SnO 2 (ZTO) thin films by e-beam evaporation technique, Appl. Phys. A 124 (2018) 1–8.
[54] L. Xu, X. Luo, H. Qian, G. Zheng, F. Xian, J. Su, Deposition and characterization of Zn–Sn–O (ZSO) thin films with novel optical properties, physica status solidi (a) 219 (8) (2022) 2100651.
[55] S.M. Abed, S.M. Mohammad, Z. Hassan, A. Muhammad, S. Rajamanickam, K. Ali, Comparative study of UV-ZnO NRs photodetectors based on seeded porous silicon by RF-sputtering and drop-casting methods, J. Mater. Sci. Mater. Electron. (2022) 1–21.
[56] S.M. Mohammad, S. Rajamanickam, Z. Hassan, M. Abdullah, A. Shafiqa, A. Abuelsamen, Self-powered UV photodetector performance optimization based on Ag nanoparticles-encapsulated-ZnO nanorods by photo-deposition method, Sensor Actuator Phys. 331 (2021) 113032.
[57] S.F. Akhtarianfar, A. Khayatian, R. Shakernejad, M. Almasi-Kashi, S.W. Hong, Improved sensitivity of UV sensors in hierarchically structured arrays of network-loaded ZnO nanorods via optimization techniques, RSC advances 7 (51) (2017) 32316–32326.
[58] J. Agrawal, T. Dixit, I. Palani, V. Singh, Development of reliable and high responsivity ZnO-based UV-C photodetector, IEEE J. Quant. Electron. 56 (1) (2019) 1–5.
[59] H. Hakkoum, A. Moumen, M. Ghougali, N. Sengouga, E. Comini, The effect of structural characteristics of ZnO and NiO thin films on the performance of NiO/ZnO photodetectors, J. Mater. Sci. Mater. Electron. 33 (35) (2022) 26604–26618.
[60] P.-H. Hsiao, T.-C. Wei, C.-Y. Chen, Stability improvement of Cu (ii)-doped ZnS/ZnO photodetectors prepared with a facile solution-processing method, Inorg. Chem. Front. 8 (2) (2021) 311–318.
[61] K. Ozel, A. Yildiz, High-detectivity ultraviolet-B photodetector based on SnO2 thin film/Si heterojunction, Semicond. Sci. Technol. 36 (9) (2021) 095001.